Numerical simulation of synthetic jet flow field and parameter analysis of actuator

LUO Zhen-bing, XIA Zhi-xun, HU Jian-xin, ZHAO Jian-min, MIAO Wan-bo, WANG De-quan

(Inst. of Aerospace and Material Engineering, National Univ. of Defence Technology, Changsha 410073, China)

Abstract: Modeling a computing model for synthetic jet actuator, X-L Model, it considers the actuator cavity, the exit throat, and the external flow field as a single computational region. Numerical computations are performed for different cases. With a view of providing references for designing a robust synthetic jet actuator, the effect of forcing factors and actuator geometric parameters on the synthetic jet is analyzed, using a priori given velocity profile at the actuator exit. A parameter correlation function of the actuator is presented to express the correlation between the synthetic jet maximal velocity and the actuator parameters.

Key words: Synthetic jet$^+$; Exciter; Numerical simulation; Model; Parameter analysis$^+$; Correlation property

合成射流流场数值模拟及激励器参数分析*

罗振兵，夏智勋，胡建新，赵建民，缪万波，王德全

(国防科技大学 航天与材料工程学院，湖南 长沙 410073)

摘 要：建立了将合成射流激励器腔体、出口喉道及外部受控流场作为单连域计算处理的全流场计算模型——X-L 模型，并进行了二维数值计算。基于数值计算获得的激励器出口数度分布，对合成射流激励器结构参数及驱动因素对合成射流的影响进行了分析，得到了表示激励器参数和出口最大速度关系的相关函数，为设计强劲且高效率的合成射流激励器提供参考。

关键词：合成射流$^+$；激励器；数值仿真；模型；参数分析$^+$；相关特性

中图分类号：V211.3 **文献标识码**：A **文章编号**：1001-4055 (2004) 03-0199-07

1 Introduction

Of all the active flow control actuators currently being studied, there has been a great deal of attention paid to one particular type of actuator, the synthetic jet (SJ) actuator. A schematic of a synthetic jet actuator and a photograph of actuators are shown in fig. 1. A typical synthetic jet, also known as a zero net mass flux device, uses a vibrating diaphragm to drive oscillatory flow through a small orifice or slot. Although there is no source, a mean jet flow is established a few diameters from the orifice due to entrained fluid, thus making SJ actuators suitable for extensive of applications.

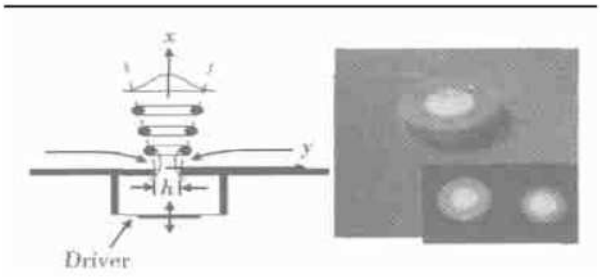

Fig. 1 Schematic of synthetic jet[1] and photograph of actuators[2]

Such actuators were previously investigated for flow control of various configurations and the results are very promising, especially for separation control, mixing en-

* 收稿日期：2003-09-16；修订日期：2003-12-01。
基金项目：国家自然科学基金重大研究计划资助项目 (90205016)；国家自然科学基金项目 (50176055)。
作者简介：罗振兵 (1979—)，男，博士生，研究领域为合成射流应用技术及固体火箭技术。
E-mail: luozhenbing@163.com

hancement and fluidic thrust vectoring, this emerging technology has received a great amount of attention from the fluid dynamics community.[1,3~8] CFD is up to now the main analytical tool for the flow control problem using SJ actuators. Several numerical studies of the actuator simulation using CFD analysis were performed. Ref.[9] solved a boundary-value problem, an simple analytic velocity profile was assumed at the orifice exit, but the computational domain encompassed only the region external to the jet without the cavity or the exit throat. Rizzetta et al.[10] used direct numerical simulation (DNS) to solve the unsteady N-S equations, the external region, the cavity, and the throat were calculated on separate grids. However, there is still a wide range of geometric parameters and the forcing factors left examine.

This paper presents the numerical results and the tools used in order to investigate the flow-field generated by the actuator under several operating conditions, and then the forcing factors and the actuator geometry are analyzed to provide references for the actuator preliminary design.

2 Numerical analysis

2.1 Governing equations

An incompressible flow solver, INS2D, developed by Rogers, et al[11] and Rogers, et al[12] is used for the simulations. An incompressible code has the advantage of running more efficiently than a compressible code, since compressible which codes run at very low Mach numbers require very small time steps to maintain stability. Accordingly, the unsteady, incompressible, Reynolds-averaged N-S (RANS) equations are solved.

The incompressible governing equations are the conservation of mass and momentum given by the continuity equation,

$$\Delta \cdot \bar{u} = 0$$

and the N-S equations in Reynolds-averaged form,

$$\rho \frac{\partial \bar{u}}{\partial t} + \rho \bar{u} \cdot \Delta \bar{u} = - \Delta \bar{p} + (\mu_1 + \mu_t) \Delta^2 \bar{u}$$

where the overbar "–" represents a Reynolds averaged quantity. The equations are solved in a time accurate manner using the method of pseudo-compressibility. With this method, subiterations are required to satisfy the continuity equation at each time step. An upwind differencing scheme based on flux-difference splitting is used to compute the convective terms. Second-order implicit scheme was used in the results reported here. The equations are solved using a generalized minimum residual scheme. The viscous fluxes are differenced using first-order accuracy. This solution scheme is stable and is capable of running at large time steps in pseudo-time, leading to fast convergence for each physical time step.

2.2 Actuator model —X-L model

At the actuator orifice exit, the velocity profile induced with SJ actuators is a function of the actuator operating parameters and geometric parameters. The profiles can be very different than a simple profile but change occurs with the interaction of the actuator-induced flow with external flow. So, in the new actuator model, the computational domain must encompass the region external to the jet, the cavity, and the exit throat. The vibrating membrane is the only moving part.

Fig. 2 is a sketch map of vibrating membrane, (x_1, l) is an arbitrary point on the membrane, the velocity of this point is composed of axial velocity $u_x(l,t)$ and radial velocity $u_l(l,t)$. If $u(t)$ is the velocity of the membrane center, we can define:

$$u_x(l,t) = \Phi(l) \cdot u(t),\ u_l(l,t) = \Psi(l) \cdot u(t) \quad (1)$$

$$u(t) = x\dot{>},\ u_x(l,t) = x\dot{>},\ u_l(l,t) = \frac{\mathrm{d}(\Delta l)}{\mathrm{d}t} \quad (2)$$

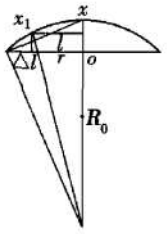

Fig. 2 Sketch map of vibrating membrane

Analyzing fig. 2, the following equations can be obtained by law of sines:

$$\frac{x}{r} = \frac{r}{2R_0 - x}, \quad \frac{x - x_1}{l} = \frac{l}{2R_0 - (x - x_1)}$$

$$\Delta l / x_1 = l / [2R_0 - (x - x_1)] \quad (3)$$

where R_0 is a curvature radius of the metal membrane.

On account of $x_1/R_0 \leq x/R_0 \approx 0 = 1$, the function (2) becomes:

$$x \approx r^2/2R_0,\ x_1 \approx (r^2 - l^2)/2R_0,\ \Delta l \approx 0 \quad (4)$$

By integrating functions (1), (2), and (3), we can make a conclusion, that is:

$$\Phi(l) \approx 1-(l^2/r^2), \quad \Psi(l) \approx 0 \tag{5}$$

The actuator membrane is excited by voltage. The perturbation displacement of the membrane center is induced as follows:

$$x(t) = A\cos(2\pi ft + \Phi_0) \tag{6}$$

where f is a forcing frequency, A denotes the amplitude of the vibrating metal membrane, and Φ_0 is the original phase of actuator membrane.

By integrating functions (1), (5), and (6), we can make a conclusion, that is:

$$u(t) = -2\pi fA \cdot \sin(2\pi ft + \Phi_0) \tag{7a}$$

$$u_x(l,t) = \Phi(l) \cdot u(t), \quad \Phi(l) \approx 1-(l^2/r^2) \tag{7b}$$

$$u_l(l,t) = \Psi(l) \cdot u(t), \quad \Psi(l) \approx 0 \tag{7c}$$

Functions (7) are a computing model for synthetic jet actuator, X-L model; it considers the actuator cavity, the exit throat, and the external flow field as a single computational region.

In this paper, $\Phi(l) \approx 1$ and $\Phi_0 = 0$, and $U_0 \cdot -2\pi fA$, then the function (7) becomes:

$$u_x(l,t) = u(t) = U_0 \cdot \sin 2\pi ft, \quad u_l(l,t) = 0 \tag{8}$$

The boundary condition on the pressure at a solid membrane surface is given by:

$$\frac{\partial \bar{p}}{\partial x} = -\rho \frac{\partial \bar{u}_n}{\partial t} \tag{9}$$

The simulation is made for both the actuator's cavity and the surrounding domain.

3 Results and analysis

3.1 Computational cases

Based on the blowing/suction type boundary condition, a host of computations of an isolated synthetic jet actuator are performed. For brevity, we discuss representative cases and the computational cases are summarized in table 1. The baseline values are $f_1 = 2$kHz, $U_{01} = 1$m/s, $h_1 = 0.5$mm, $d_1 = 0.5$mm, $H_1 = 5$mm and $D_1 = 2$mm。

The computational domain and grid of synthetic jet actuator for the baseline case (case1) are illustrated in fig. 3. Table 2 provides detail domain sizes and grid distributions for the baseline case (case1).

The synthetic jet velocity vector maps for case1 ~ 21 are shown in fig. 4.

Table 1　Computational cases for synthetic jet actuators

Case	f/f_1	U_0/U_{01}	h/h_1	d/d_1	D/D_1	H/H_1
Case1	1	1	1	1	1	1
Case2	0.25	1	1	1	1	1
Case3	0.5	1	1	1	1	1
Case4	2	1	1	1	1	1
Case5	1	0.25	1	1	1	1
Case6	1	0.5	1	1	1	1
Case7	1	2	1	1	1	1
Case8	1	1	0.2	1	1	1
Case9	1	1	0.5	1	1	1
Case10	1	1	2	1	1	1
Case11	1	1	1	0.2	1	1
Case12	1	1	1	0.5	1	1
Case13	1	1	1	4	1	1
Case14	1	1	1	1	0.5	1
Case15	1	1	1	1	3.0	1
Case16	1	1	1	1	1	0.2
Case17	1	1	1	1	1	0.5
Case18	1	1	1	1	1	2
Case19	1	1	1	1	3	1
Case20	1	1	1	1	3	1
Case21	1	1	1	1	3	1

Note: In case19, 20, 21, the orifice lip geometry is: a flat lip, a rounded lip and a cusp-shaped lip.

Table 2　Computational domain and grid distribution

Designation	Domain	Grid	Remark
Cavity	2 × 5	40 × 100	Dense in center
Nozzle	0.5 × 0.5	20 × 20	Divided evenly
External	15 × 7.5	150 × 100	Dense in center

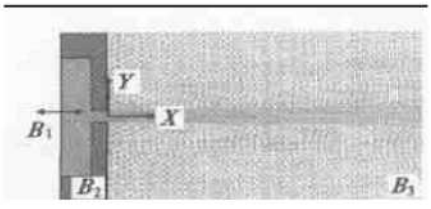

Fig. 3　Computational domain and grid of synthetic jet actuator

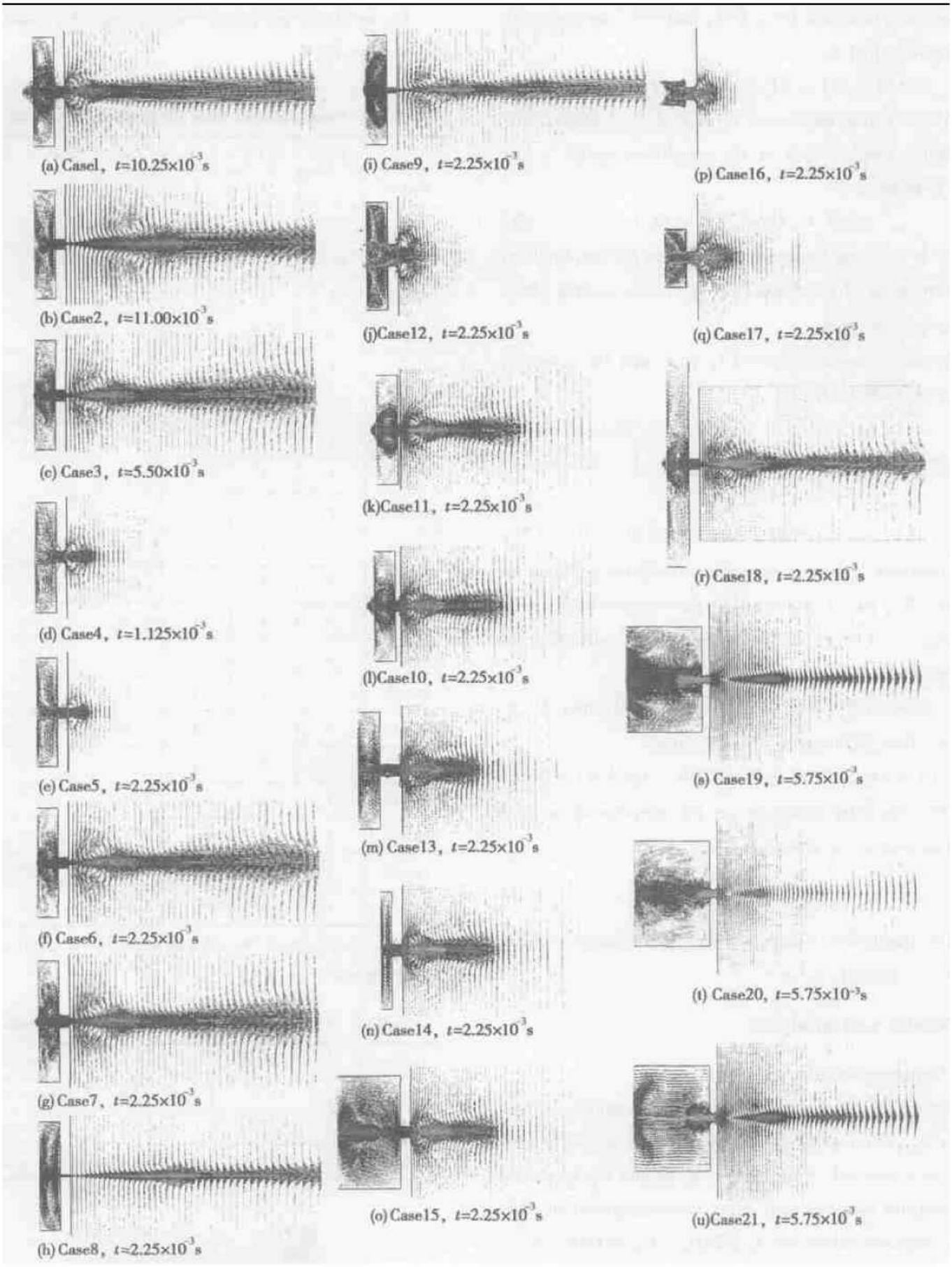

Fig. 4 Synthetic jet velocity vector maps for different cases

3.2 Effect of forcing factors

The performance of synthetic jet is determined by several parameters. Evidently, once the actuator geometry is set, the forcing factors of membrane play a fundamental

role. The forcing factors are: the forcing amplitude and the forcing frequency.

3.2.1　Effect of the forcing amplitude

The relation function between the vibrating velocity amplitude (U_0) and the driving amplitude (A) of the metal membrane is:

$$U_0 \bullet - 2\pi fA \tag{10}$$

when the driving frequency is definite, we can use U_0 to denote A .

The actuator was operated at four amplitudes: 1m/s, 0.25m/s, 0.5m/s and 2m/s (case 1, case 5, case 6, and case 7 correspondingly). The velocity vector maps are illustrated in fig.4(a), (e), (f), (g), exhibit a high sensitivity to the driving amplitude. Fig.5 shows that the synthetic jet maximal velocity u_m is almost in direct proportion to the vibrating velocity amplitude U_0, that is to say:

$$u_{\mathrm{m}} \propto A \tag{11}$$

3.2.2　Effect of the forcing frequency

In order to study the effect of driving frequency, the actuator was simulated at four frequencies: 2kHz, 500Hz, 1kHz and 4kHz (case1, case2, case3, case4). In these cases, the amplitude U_0 is set, we can see that the membrane amplitude A is a variable from the equation (11).

The velocity vector maps for different forcing frequencies are presented in fig.4(a) ~ (d), they also show a high sensitivity to the driving frequency. When the synthetic jet is studied by reducing the driving frequency to 1/2 (case3) of the original baseline case (case1), the membrane amplitude A also lowers to 1/2 of the original. fig.6 shows that the synthetic jet maximal velocities u_{m} are equal for case1 and case3. By integrating functions (10) and (11), we can make a conclusion, that is:

$$u_{\mathrm{m}} \propto f \tag{12}$$

When the forcing frequency is greater than a forky frequency f_{c}, u_{m} drops rapidly with increasing the forcing frequency. For example, doubling the forcing frequency of the original baseline case, the synthetic jet maximal velocity u_{m}(case4) is dramatically reduced, and there is almost no jet at the exit downstream, which is shown in fig.4(d) and fig.6. Essentially, the synthetic jet is a train of vortices. During the blow phase, a vortex pair, or ring, is formed, reaches its maximum strength and moves away from the orifice under the action of self-induction. When the jet begins its suction cycle, the vortex ring will continue to move away from the exit plane of the actuator and behind the ring, the ambient fluid is drawn into fill the cavity. If the forcing frequency is too high, the vortex ring will not reach its maximum strength and will be drawn into the cavity during the suck. So the function (12) is restricted, and becomes as follows:

$$u_{\mathrm{m}} \propto f \ , \ f \leq f_{\mathrm{c}} \tag{13}$$

where $1\mathrm{kHz} \leq f_{\mathrm{c}} \leq 2\mathrm{kHz}$.

3.3　Study of geometric parameters

With a view to providing references for the actuator preliminary design, the effects of varying the cavity depth, the membrane width, the orifice width, the orifice depth, and the orifice lip geometry are investigated.

3.3.1　Orifice size and orifice depth

Synthetic jet velocity vector maps for different orifice sizes are shown in fig.4(h) ~ (j). When the orifice size (or width) increases (case8~ 10), comparison with case1 indicates some significant difference. Synthetic jet centerline velocity profiles for different orifice sizes are shown in fig.7. As the orifice size is increases, the SJ centerline velocity reduces significantly. For example, when the orifice size increases from $h_1 = 0.25\mathrm{mm}$ (case9) to $h_1 = 0.5\mathrm{mm}$ (case1), the centerline velocity u profile decreases by 100%. This phenomenon is related to the redistribution of total momentum over a large area. Fig.7 shows that the synthetic jet maximal velocity u_m is almost in inverse proportion to the orifice size (or width) h, that is:

$$u_{\mathrm{m}} \propto 1/h \tag{14}$$

The velocity vector maps for different orifice depths are presented in fig.4(k) ~ (m). When the orifice depth decreases (case11~ 13), the centerline velocity u profile increases as shown in fig.8. When the orifice depth is doubled, the centerline velocity u profile almost decreases by 20%. This result is entirely not surprising: as the orifice depth increases, the viscous dissipation begins to dominate, and the peak velocity drops.

3.3.2　Cavity depth and membrane width

Sensitivity of the SJ flow to the size of the internal cavity is studied by changing the cavity depth (case14~ 15) and the membrane width (case16~ 18).

The velocity vector maps for different cavity depths are presented in fig. 4(n) and 4(o) . Fig. 9 shows the centerline velocity profiles for different cavity depths. Decreasing (case14) or increasing (case15) the cavity depth does not appreciably affect the external flow field.

The velocity vector maps for different membrane widths are presented in fig. 4(p) ~ (r) , they demonstrate that the larger the actuator membrane width, the higher the exit synthetic jet velocity. Fig. 10 shows that the synthetic jet maximal velocity u_m is almost in direct proportion to the membrane width H, that is:

$$u_m \propto H \tag{15}$$

3.3.3 Lip geometry

To examine the effect of the lip geometry on the flow, three types of lips are used: a flat lip, a round lip, and a cusp-shaped lip as shown schematically on the lower right of fig. 11. The jet velocity vector maps for different lip geometries are presented in fig. 4(s) ~ (u) and centerline velocity profile are shown in fig. 11 (case19~ 21) . The geometry of the actuator exit lip has less effect on the synthetic jet velocity. At the same condition, the exit velocity of the flat lip actuator is the highest and the synthetic jet is centralized. Conversely, the exit velocity of the round lip actuator is the lowest and the synthetic jet is dispersed. The reason is the round lip allows more fluid to flow out the cavity from the spanwise side during a blowing phase, causing the decrease in the stream wise velocity and the increase in the spanwise velocity.

3.4 Parameter correlation function

From the above results, conclusions and function (11) , (13) , (14) , (15) , a parameter correlation between the synthetic jet maximal velocity u_m and the other parameters, such as the forcing factors and the geometric parameters, can be defined as

$$u_m = kfA(H/h) \cdot \Phi(d, Lip) \quad f \leq f_c \tag{16}$$

where k is a correction coefficient, $\Phi(d, Lip)$ depicts the effect of the orifice depth and the lip geometry.

The parameter correlation function (16) reveals the possibility of enhancing the actuator performance and making a robust actuator through designing driving factors and

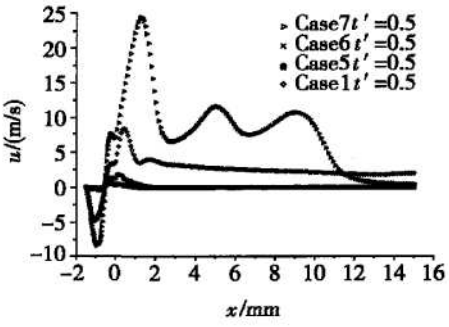

Fig. 5 Centerline velocity profiles for different forcing amplitudes

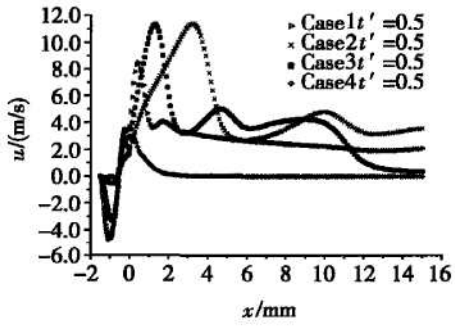

Fig. 6 Centerline velocity profiles for different forcing frequencies

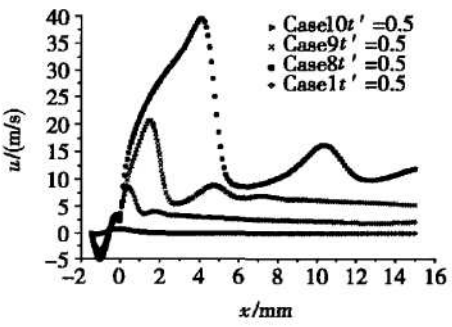

Fig. 7 Centerline velocity profiles for different orifice widths

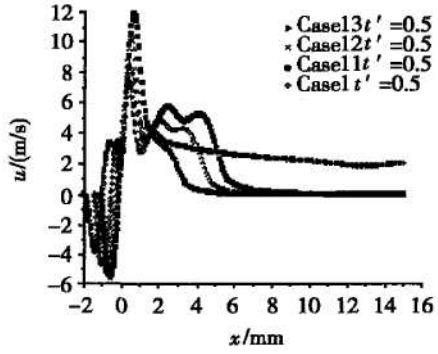

Fig. 8 Centerline velocity profiles for different orifice depths

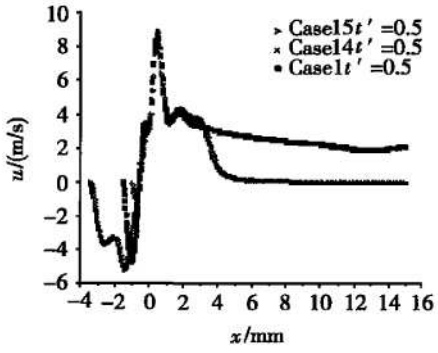

Fig. 9 Centerline velocity profiles for different cavity depths

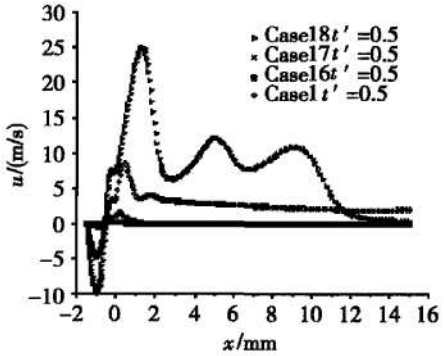

Fig. 10 Centerline velocity profiles for different membrane widths

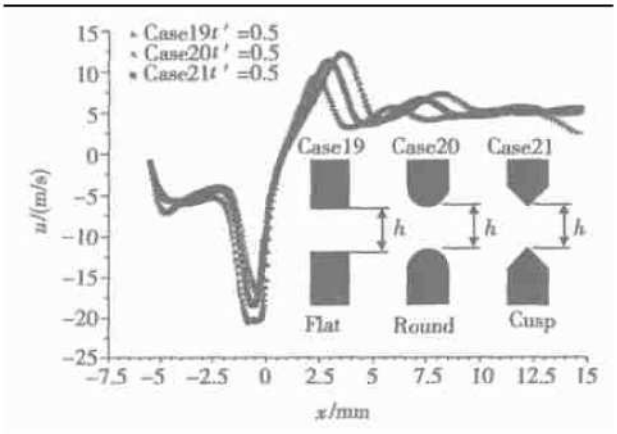

Fig. 11　Centerline velocity profiles for flat, cusp and round lips

geometric parameters.

If we take the fluid properties into account, the parameter correlation function (16) may be expressed as

$$u_m = kfA(H/h) \cdot \Phi(d, Lip) \cdot \Psi(\mu) \quad f \leq f_c \quad (17)$$

where $\Psi(\mu)$ denotes the effect of the fluid properties on the synthetic jet.

4　Conclusions and future work

(1) The synthetic jet maximal velocity is almost in direct proportion to the membrane vibrating amplitude.

(2) If the forcing frequency is restricted, the synthetic jet maximal velocity is also in proportion to the forcing frequency. However, when the forcing frequency excesses the restricting frequency, the jet maximal velocity will drop rapidly, and there is almost no jet at the exit downstream for a higher frequency.

(3) The synthetic jet was observed to be highly sensitive to the membrane width and the orifice width. The larger the ratio of the membrane area to the actuator exit area, the higher the exit synthetic jet velocity.

(4) The depth of the actuator cavity has hardly any effect on the synthetic jet, but the depth of the actuator exit is an important parameter in resulting flow. Commonly, the deeper the actuator exit, the higher the actuator exit velocity is.

(5) The orifice lip geometry is also found to be an important parameter in resulting flow. At the same condition, the exit velocity of the flat lip shape actuator is the highest and the synthetic jet is centralized. Conversely, the exit velocity of the round lip actuator is the lowest and the synthetic jet is dispersed.

The above conclusions can be defined by a correlation function $u_m = kfA(H/h) \cdot \Phi(d, Lip)$, $f \leq f_c$. This function indicates the possibility of enhancing the actuator performance and making a robust actuator by designing driving factors and geometric parameters.

References:

[1] Smith B L, Glezer A. Vectoring and small-scale motions effected in free shear flows using synthetic jet actuators[R]. *AIAA* 97-0213.

[2] LUO Zhen-bing. Mechanism and application investigation of synthetic jet[D]. *Master Thesis*, *National Univ. of Defense Technology*, 2002.

[3] LUO Zhen-bing, XIA Zhi-xun, FANG Ding-you. The factors influencing the synthetic jet[J]. *Journal of National University of Defense Technology*, 2002(4).

[4] Seifert A, Pack L G. Oscillatory excitation of compressible flows over airfoils at flight Reynolds numbers[R]. *AIAA* 99-0925.

[5] Amitay M, Smith B L, Glezer A. Aerodynamic flow control using synthetic jet technology[R]. *AIAA* 98-0208.

[6] Nae C. Synthetic jets influence on NACA 0012 airfoil at high angles of attack[R]. *AIAA* 98-4523.

[7] LUO Zhen-bing, XIA Zhi-xun, HU Jian-xin, et al. Enhancing fuel/oxygen mixing using synthetic jet actuators[J]. *Journal of Propulsion Technology*, 2003(2). (罗振兵, 夏智勋, 胡建新, 等. 应用合成射流技术增强燃气/氧气掺混[J]. 推进技术, 2003, 24(2).)

[8] Nae C. Unsteady flow control using synthetic jet actuators[R]. *AIAA* 2000-2403.

[9] Kral L D, Donovan J F, Cain A B, et al. Numerical simulation of synthetic jet actuators[R]. *AIAA* 97-1824.

[10] Rizzetta D P, Visbal M R, Stanek M J. Numerical investigation of synthetic jet flowfields[R]. *AIAA* 98-2910.

[11] Rogers S E, Kwak D. An upwind differencing scheme for the time-accurate incompressible Navier-Stokes equations[J]. *AIAA Journal*, 1990, 28(2).

[12] Rogers S E, Kwak D, Kiris C. Steady and unsteady solutions of the incompressible Navier-Stokes equations[J]. *AIAA Journal*, 1991, 29(4).

[13] Kral L D, Mani M, Ladd J A. Application of turbulence models for aerodynamic and propulsion flow fields[J]. *AIAA Journal*, 1996, 34(11).

(编辑: 王居信)